Supplementary Information (SI) for Energy & Environmental Science.

Supporting Information

Biomimetic bone hydrogel enables seamless interface for aqueous battery and human/machine interaction

Lingbo Yao[1,2], Yichao Wang[1,2], Lvzhang Jiang[1,2], Gege Wang[1,2], Xiaowei Chi[1*], Yu Liu[1*]

[1]Shanghai Institute of Ceramics, Chinese Academy of Sciences
Shanghai 200050, China

[2]University of Chinese Academy of Sciences
Beijing 100049, China

*Email: xwchi@mail.sic.ac.cn; yuliu@mail.sic.ac.cn

Experimental Section

Preparation of BBH electrolytes: First, 0.2 g HA (AR, Aladdin) was added to the mixed solvent of 8 g deionized water, 2 g anhydrous ethanol, and 0.2 g glycerol before intense mixing through magnetic stirring. After complete dispersion, 1 g gelatin (AR, Aladdin, ~250 g Bloom) and 0.2 g CMCS (AR, Shanghai yuanye Bio-Technology Co., Ltd) were added to the as-prepared dispersion solution with HA under an 80 °C water bath stirring for 3 h. After that, the hot BBH precursor solution was poured into the PTFE mold of $10\times10\times0.1$ cm^3 rapidly and transferred into the low-temperature box under -20 °C for 1 h. Finally, the BBH electrolytes were obtained after soaking the air-drying BBH membrane with the 3 m $ZnSO_4$, 0.5 m K_2SO_4+1 m $ZnSO_4$, or 2 m Li_2SO_4+1 m $ZnSO_4$ electrolytes.

Preparation of GCH electrolytes: First, 1 g gelatin and 0.2 g CMCS were added to the 10 g deionized water under an 80 °C water bath stirring for 3 h. After that, the hot GCH precursor solution was poured into the PTFE mold of $10\times10\times0.1$ cm^3 rapidly and stand in the 25 °C air environment for 24 h. Finally, the GCH electrolytes were obtained after soaking the air-drying GCH membrane with the 3 m $ZnSO_4$, or 0.5 m K_2SO_4+1 m $ZnSO_4$ electrolytes.

Preparation of GH electrolytes: First, 1 g gelatin was added to the 10 g deionized water under an 80 °C water bath stirring for 3 h. After that, the hot precursor solution was poured into the PTFE mold of $10\times10\times0.1$ cm^3 rapidly and stand in the 25 °C air environment for 24 h. Finally, the gelatin electrolytes were obtained after soaking the air-drying gelatin membrane with the 3 m $ZnSO_4$ electrolytes.

Preparation of PAM hydrogels: First, 2 g of acrylamide was added to the 10 g deionized water under an 80 °C water bath stirring for 1 h. After that, 0.02 g of N, N-Methylene-bis-acrylamide and 0.02 g of Irgacure-2959 were added into the solution as prepared before stirring for 10 min. After that, the solution was poured into the glass mold of 10×10×0.1 cm^3 rapidly under UV irradiation for 20 min. Finally, the PAM hydrogel was obtained.

Preparation of BBHS and in-situ gelation process: To prepare the precursor solution of BBHS, 0.2 g HA was added to the mixed solvent of 8 g deionized water and 2 g glycerol before an 80 °C water bath stirring for dispersion. After that, 0.2 g CMCS and 2 g gelatin were added to the as-prepared solution at 80 °C with stirring for 12 h. After that, keep stirring the solution at 50 °C for backup. Finally, the flexible BBHS-based interface can be formed by spreading the BBHS precursor solutions on the skin surface and standing for several minutes under treatments of different temperatures.

Preparation of BBHS Sensors: To prepare the BBHS Sensors, 0.2 g HA and 0.584 g NaCl were added to the mixed solvent of 7 g deionized water, 1 g glycerol, and 2 g anhydrous ethanol before an 80 °C water bath stirring for dispersion. After that, 0.2 g CMCS and 2 g gelatin were added to the as-prepared solution at 80 °C and keep stirring for 12 h. Finally, the flexible BBHS Sensors were fabricated by spreading the BBHS precursor solutions on the Ag/AgCl electrodes attached to the adhesive bandage at -20 °C for 10 min and stand at room temperature for 6 h before using.

Preparation of GCHS Sensors: To prepare the GCHS Sensors, 0.584 g NaCl were added to 10 g deionized water. After complete dissolution, 0.2 g CMCS and 2 g gelatin were added to the as-prepared solution at 80 °C and keep stirring for 12 h. Finally, the flexible BBHS Sensors were fabricated by spreading the BBHS precursor solutions on the Ag/AgCl electrodes attached to the adhesive bandage at -20 °C for 10 min and stand at room temperature for 6 h before using.

Preparation of ZnHCF cathodes: The ZnHCF was prepared through a coprecipitation reaction strategy[1]. 50 ml of solution containing 1.89 g $Zn(NO_3)_2 \cdot 6H_2O$ (AR, Aladdin) was added to a 100 ml solution containing 1.27 g $K_3Fe(CN)_6 \cdot H_2O$ (AR, Aladdin), drop by drop under stirring at 60 °C for 2 h. The obtained solution was aged for 12 hours. The precipitate was collected by centrifugation and washed three times with water and pure ethanol, respectively. The washed solid product was then dried at 100 °C for 12 h.

The ZnHCF cathode was then prepared by mixing 70 wt.% of ZnHCF, 10 wt.% of Super P, and 10 wt.% of PVDF as the binder in NMP solvent and cast onto a Ti foil and dried for 12 h at 70 °C.

***Preparation of LMO cathodes**:* The commercial $LiMn_2O_4$ powders (Canrud) were directly used for the preparation of LMO cathodes. The LMO cathode was prepared by mixing 70 wt.% of LMO, 10 wt.% of Super P, and 10 wt.% of PVDF as the binder in NMP solvent and cast onto a Ti foil and dried for 12 h at 100 °C. The high mass-loading LMO cathodes were prepared by the mixing of LMO, Super P, and PTFE emulsion (60 wt.%) with a mass ratio of 7:2:1. After emulsion breaking by the absolute ethanol, the mixture dough was rolled onto the Ti collector.

Materials characterization: The tensile strength and tear strength tests of the hydrogels were conducted on a universal material testing machine (Instron-5592) with the unified standard specimens. All the specimens were stretched along the length direction at an extension rate of 100 mm min^{-1}. The nanoindentation hardness was characterized on a nanoindentation instrument (Bruker Hysitron TI980). The micro-CT imaging was conducted by GE Vtomex system with a scanning voltage of 30 kV, current of 50 μA, and resolution of 2 μm. The pore structures were tested by the mercury intrusion instrument (Micromeritics Autopore V 9620). The thermal properties of hydrogels were characterized by a thermogravimetric analyzer (TGA, NETZSC, STA 409 PC) with a heating rate of 5 °C min^{-1} in the N_2 atmosphere. The electronic structure and corresponding composition were characterized by X-ray photoelectron spectroscopy (XPS, Thermo Scientific K-Alpha). Characteristic functional groups and bond structures were analyzed by the attenuated total reflection Fourier transform infrared spectroscopy (ATR-FTIR, Thermo Scientific Nicolet iS5) in the range of 4000 to 400 cm^{-1} with the resolution of 4 cm^{-1}. The ^1H NMR spectra were characterized using the heavy water as a deuterated reagent (Bruker Avance NEO 400MHz). The phase structures of hydrogels and Zn anodes were identified by X-ray diffraction (XRD, Rigaku Ultima diffractometer with Cu Kα radiation, $\lambda = 1.5418$ Å). Morphology and roughness of the Zn anodes were analyzed by optical profiler (Mahr LD130). Scanning electron microscopy (SEM, JEOL, JSM-6510) equipped with the energy dispersion spectrometer (EDS) was employed to observe the morphology and elements distribution of the hydrogels, HA, and Zn anodes. The rheological properties of the hydrogel were measured by rheometer (HAAKE MARS60) with a 20 mm diameter plater at a fixed shear rate and a heating rate of 5 °C min^{-1}. For in-situ gelation adhesion force measurement, the BBHS precursor in liquid form was dropped to the substrate and cooled to the set temperature. The peeling force at constant 90° was tested with universal material testing machine Instron-5592 at a peeling speed of 50 mm min^{-1}.

Cytotoxicity characterization: The MC3T3-E1 cells were cultured in a proliferation medium of 89% MEM-α supplemented with 10% fetal bovine serum and 1% P/S. The hydrogels were punched at a size of 6×6 mm^2, which were disinfected under ultraviolet light for 30 min. Thereafter, the hydrogels were placed in the wells of a 48-well culture plate with a density of 2×10^5 cells/well at 37 °C under 5% CO_2. CCK-8 solution of 500 μL was added to each well after co-culturing the cells with hydrogels for 48 h, and the absorbance at 450 nm were measured after 2 h. The MC3T3-E1 cells of the logarithmic growth stage were inoculated into a confocal dish with a density of 2×10^5 cells/well for co-culturing at 37 °C under 5% CO_2. After 48 h, the culture medium was removed and the wells were cleaned three times with PBS. Dilute reagent A (Calcein) and reagent B (PI) with complete culture medium at 1:1000 and 1:2000, respectively. The staining solution of 1 ml/well was added and incubated at room temperature in the dark for 15 minutes before PBS washing and observation. The cell relative viability was calculated according to the equation:

$$Cell\ relative\ viability\% = \frac{OD_{exp}}{OD_{control}}\% \qquad \text{Equation (1)}$$

Electrochemical measurement

Electrochemical impedance spectroscopy (EIS), chronoamperometry (CA), linear sweeping voltammetry (LSV), and cyclic voltammetry (CV) were performed on the electrochemical workstation (Autolab instrument PGSTAT302N). The AC signal ranging from 0.01 Hz to 1000 kHz was used for all the EIS tests. Galvanostatic charge/discharge (GCD) cycling tests were carried out on the LAND CT2100A. Tafel tests were conducted using a scanning rate of 1 mV s^{-1} with Zn as the working electrode, Zn as the counter electrode, and another Zn as the reference electrode. The DRT analysis was performed by using DRT Tools[2]. The equation of ionic conductivity (σ) was calculated by the equation:

$$\sigma = \frac{L}{RS} \qquad \text{Equation (2)}$$

where L represents the thickness of electrolyte, S is the contacting area, and R is the bulk resistance from the EIS test. The Zn transference number (t_{Zn2+}) test was tested based on Chronoamperometry test (CA). At a polarization voltage of 20 mV, the t_{Zn2+} was calculated based on the equation:

$$t_{Zn^{2+}} = \frac{I_s(\Delta V - I_0 R_0)}{I_0(\Delta V - I_s R_s)} \qquad \text{Equation (3)}$$

where I_0 and I_s are the initial and steady-state current, ΔV is the applied constant potential (20 mV), and R_0 and R_s are the initial and steady-state interface resistance, respectively.

The symmetric and full cells were assembled using commercial Zn foils (100 and 10 μm) as anodes and Ti foils as collectors. For the ZnHCF and LMO electrodes used in normal battery testing, they are both disks with a diameter of 1.4 cm and mass loading of ca. 2 mg cm^{-2}. For solid-state battery tests using HA-ZS electrolyte, the Zn||Zn symmetric battery was tested in a cylindrical mold with a diameter of 11 mm. Firstly, the zinc powders were added into the mold and cold-pressed; then, the HA-ZS electrolyte powders were uniformly dispersed onto the as-pressed zinc powders and pressed. Finally, the same amount of zinc powder was added onto the as-pressed HA-ZS electrolyte and co-pressed at 5 MPa to obtain the Zn||Zn symmetric battery. The thickness of the HA-ZS layer is close to 400 μm.

As to the details of the hot-pressing process to help the infiltration of thick electrodes, firstly, the BBH electrolyte impregnated with electrolyte was heated in a 60 °C oven for 10 minutes to soften the gelatin chain segments. Then, the BBH electrolyte was attached to the LMO electrode and quickly subjected to a constant pressure of 1 MPa for one minute to benefit the seamless infiltration of BBH into the LMO electrode. For pouch cells, the sizes of anodes and cathodes were both 3×3 cm^2.

For the LSV tests, three kinds of electrolytes were soaked with 3 M $ZnSO_4$ or 1 M Na_2SO_4 (pH=3.5) for 12 h, respectively. The Zn and C@Ti (Super P: PVDF=9:1) with a diameter of 14 mm were used as the working electrodes or counter electrodes, and another Zn electrode was used as reference electrode. The Electromyographic and Electrocardiographic profiles were tested with commercial processing circuits (Sichiray) based on the Commercial Sensors (3M) and BBHS Sensors. Tests involving human subjects were conducted with the full informed consent of the volunteers, and the biocompatible BBHS had no physiological or psychological effect on the volunteers. Specifically, the signal-to-noise ratio (SNR) calculation is based on the following equation:

$$SNR(dB) = 10 \times log_{10}\left(\frac{P_{signal}}{P_{noise}}\right) \quad \text{Equation (4)}$$

where P_{signal} represents the mean square value of the signal, P_{noise} represents the mean square value of the noise signal, which is obtained by subtracting the original signal from the smoothed signal.

Computational methods

The models for finite element analysis were designed with a 2×3 mm^2 plate. Uniformly distributed semi-ellipses with a major axis of 0.09 mm and minor axis of 0.04 mm represent the HA fillers, and a triangular defect with a height of 0.4 mm and a bottom width of 0.1 m was used as the initial crack. The set of Young’s Modulus of matrix was 5 MPa, while for the filler was 12 MPa according to the properties on collagen and bone materials. A body load of 1×10^6 N m^{-2} with unilateral fix constraint was applied. The MUMPS solver is adopted to solve the models with a less than 1×10^{-3} relative error.

The binding energies were calculated using the Gaussian (G09) program at the B3LYP-GD3BJ/6-31G(d,p) level[3-5]. The implicit universal solvation model based on Solute Electron Density (SMD) with a dielectric constant of water was employed to investigate the influence of the solvents[6]. The binding energy is calculated based on the following equation:

$$E_{be} = E_{A+B} - (E_A + E_B) \qquad \text{Equation (5)}$$

Among them, the E_{A+B} is the Gibbs free energy of combination A and B and the second item is the sum of the Gibbs free energy of individual A and B.

The adsorption energies and differential charge density were calculated using the Vienna ab initio simulation package[7]. The generalized gradient approximation function GGA-PBE was used to describe the exchange-correlation potential energy. Plane-waves were used with a cutoff energy of 500 eV and a Monkhorst-Pack of k-mesh of $3\times3\times1$ for the geometry optimization and the calculation of energy. The long-range van der Waals (dispersion) correction was considered by using a nonlocal vdW-DF functional. The structural parameters were optimized with the energy and forces converged to 1×10^{-5} and 0.02 eV Å^{-1}, respectively.

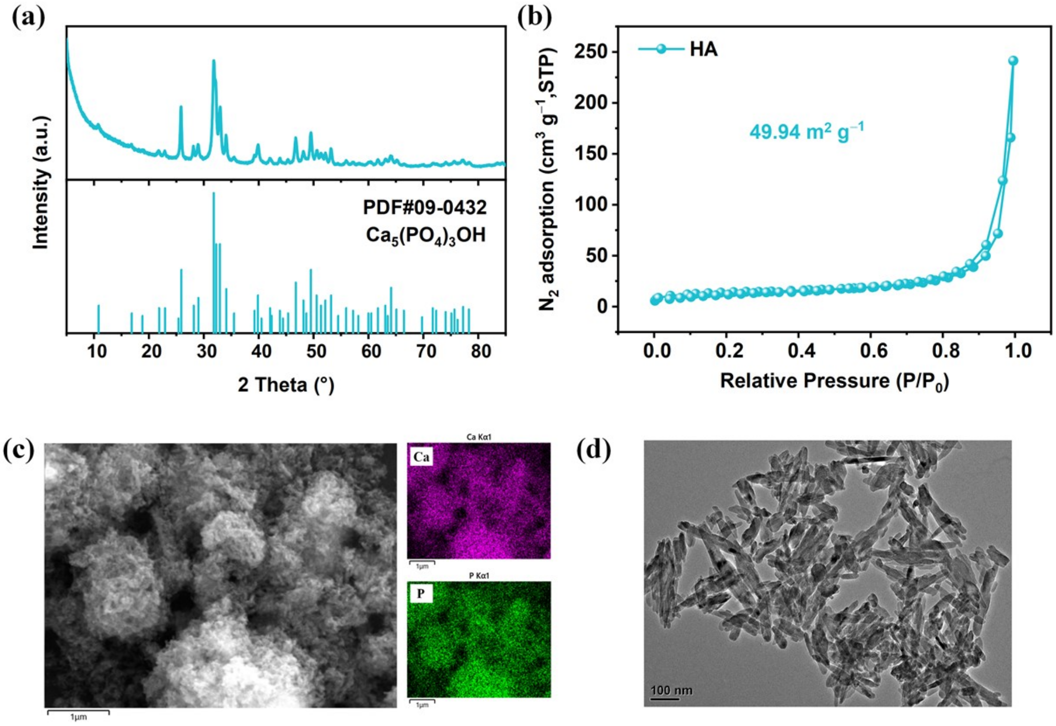

Figure S1. Structural characterization of HA nanorods. (a) XRD spectra. (b) BET tests of HA. (c) SEM images and corresponding EDS mapping of Ca and P elements. (d) TEM images.

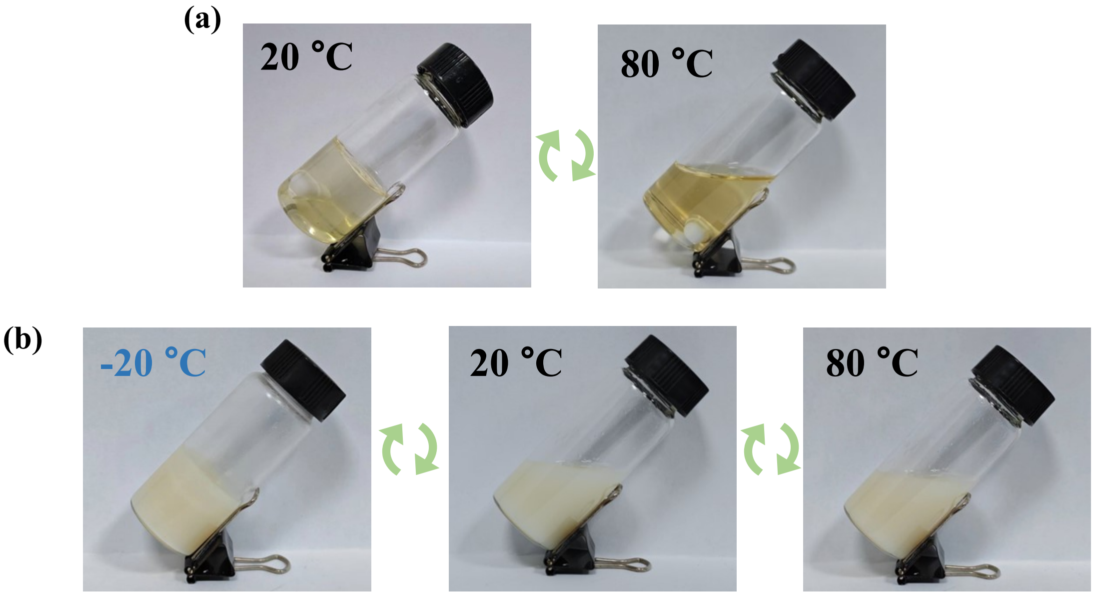

Figure S2. Thermal phase transition process of (a) GCH and (b) BBH.

Choosing a suitable hydrogel skeleton is crucial for achieving biomimetic design of bone joints. However, collagen has large molecular weight, complex structure and poor solubility, which is expensive and difficult to produce[8, 9]. Although the excessive triple helix structure is conducive to the mechanical properties of natural biological tissues, it may lead to processing difficulties and decreased uniformity in artificial bionics[9]. Gelatin is a product of partial hydrolysis of collagen, with a wide range of sources and low cost[10]. Meanwhile, the small molecular weight of gelatin facilitates rapid dissolution and formation of a uniform solution, thus facilitating efficient and uniform formation of the cross-linked three-dimensional network structure. In addition, the partially disordered structure of gelatin is closer to the flexibility and dynamic characteristics required for biomimetics, and its combination with CMCS facilitates rapid ion transport[11, 12]. All these properties make gelatin a more advantageous choice in the fields of aqueous batteries and human/machine interfaces.

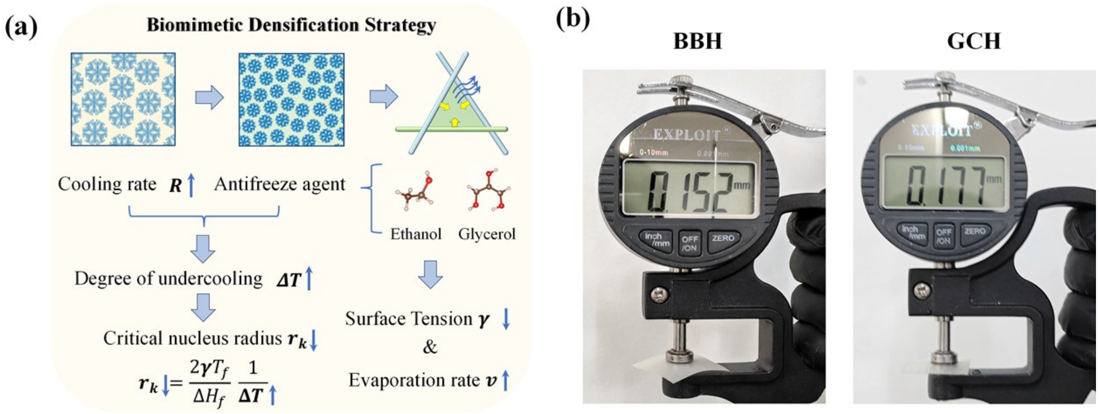

Figure S3. (a) Mechanism of regulation of ice crystal growth and chain contraction. (b) Thickness of BBH and GCH films.

The microstructure of gelatin skeleton is influenced by the freezing cross-linking process, since the cross-linking of chain segments is triggered by the nucleation and growth of ice crystals[13, 14]. The liquid region of the prepared hydrogel is derived from ice crystals, and a large number of liquid regions will lead to serious side reactions and lower mechanical strength[9, 15]. By introducing ethanol and glycerol to regulate the undercooling of sol precursors, and reducing the overall surface tension, the critical radius for ice crystal nucleation was lowered[15, 16]. In addition, the low boiling point of ethanol accelerates the subsequent chain shrinkage process, thereby achieving densification design through two aspects.

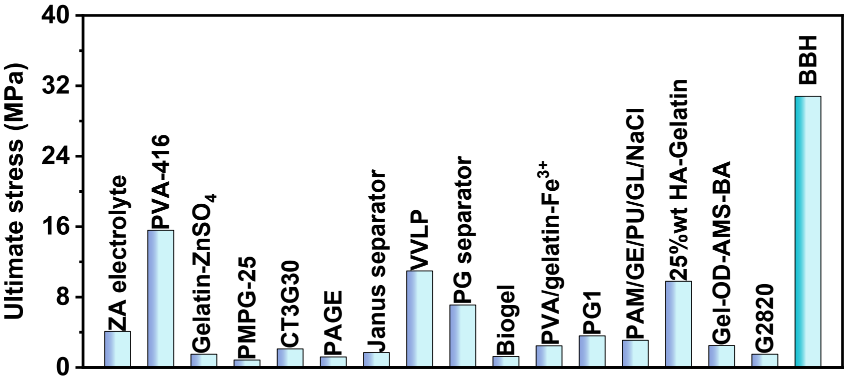

Figure S4. Comparison of ultimate strength of the hydrogels reported in the previous works[17-31].

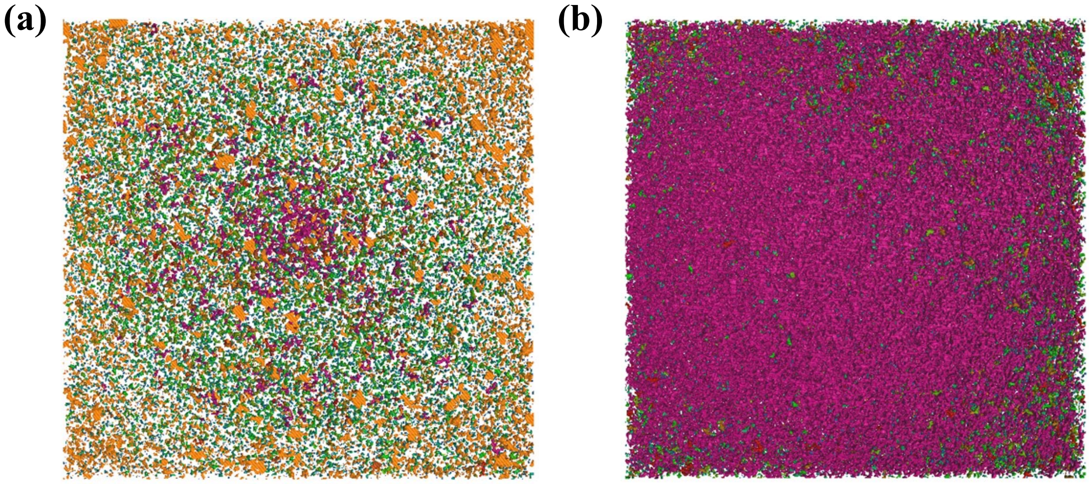

Figure S5. The structural models of (a) BBH, and (b) GCH constructed by the micro-CT scan. The orange part represents the material structure, while the green to purple part represents the pore structure.

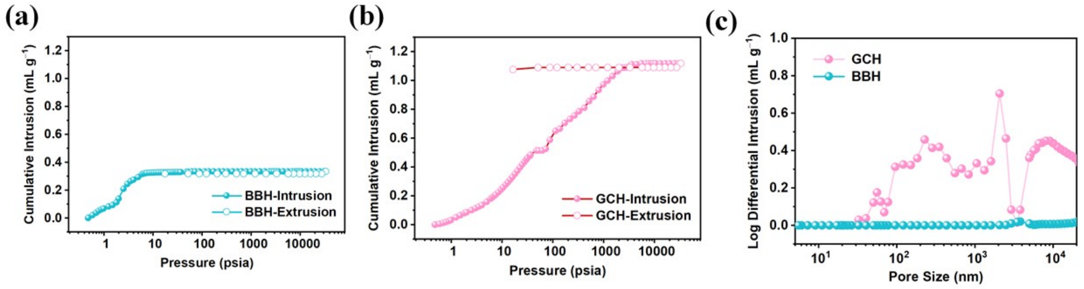

Figure S6. The mercury intrusion tests. The cumulative intrusion of frozen-dried (a) BBH, (b) GCH, and corresponding (c) pore-size distribution.

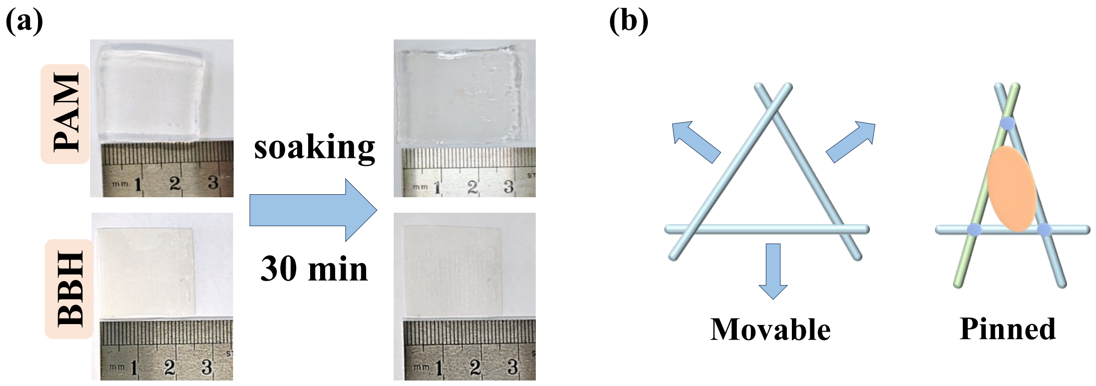

Figure S7. Structural stability of BBH. (a) Anti-swelling properties of PAM (top) and BBH hydrogel before (left) and after soaking with $ZnSO_4$-based electrolytes for 1 h. (b) Mechanism diagram of chain segment motion with/without biomimetic densification design.

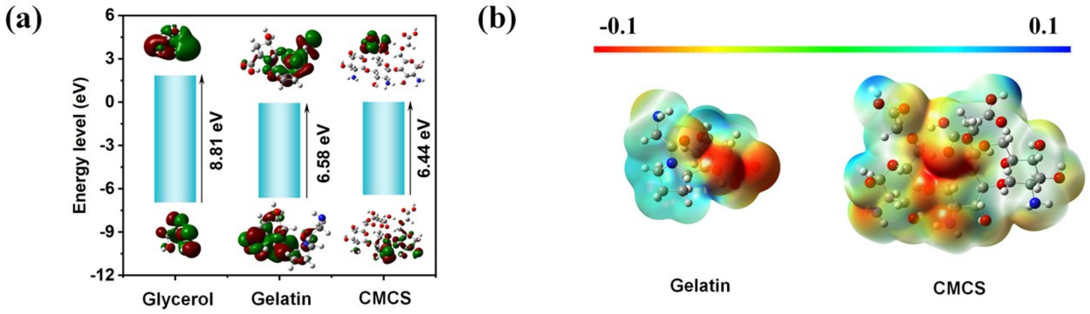

Figure S8. The DFT calculation results of the component used in the BBH. (a) Energy levels of Glycerol, Gelatin, and CMCS. (b) ESP distribution of Gelatin and CMCS.

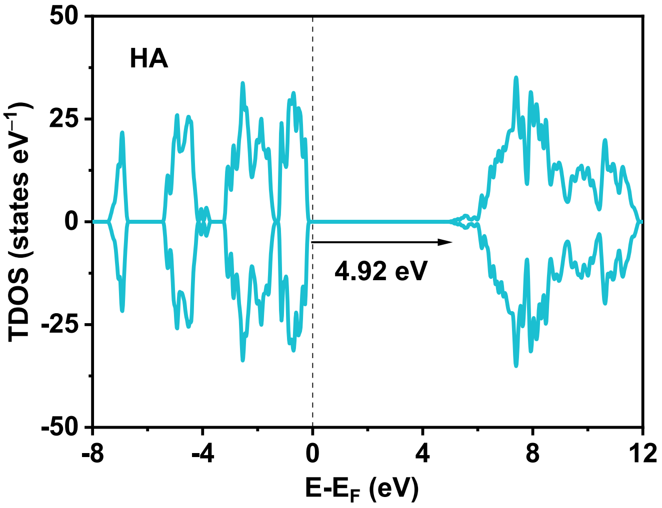

Figure S9. DOS distribution of HA.

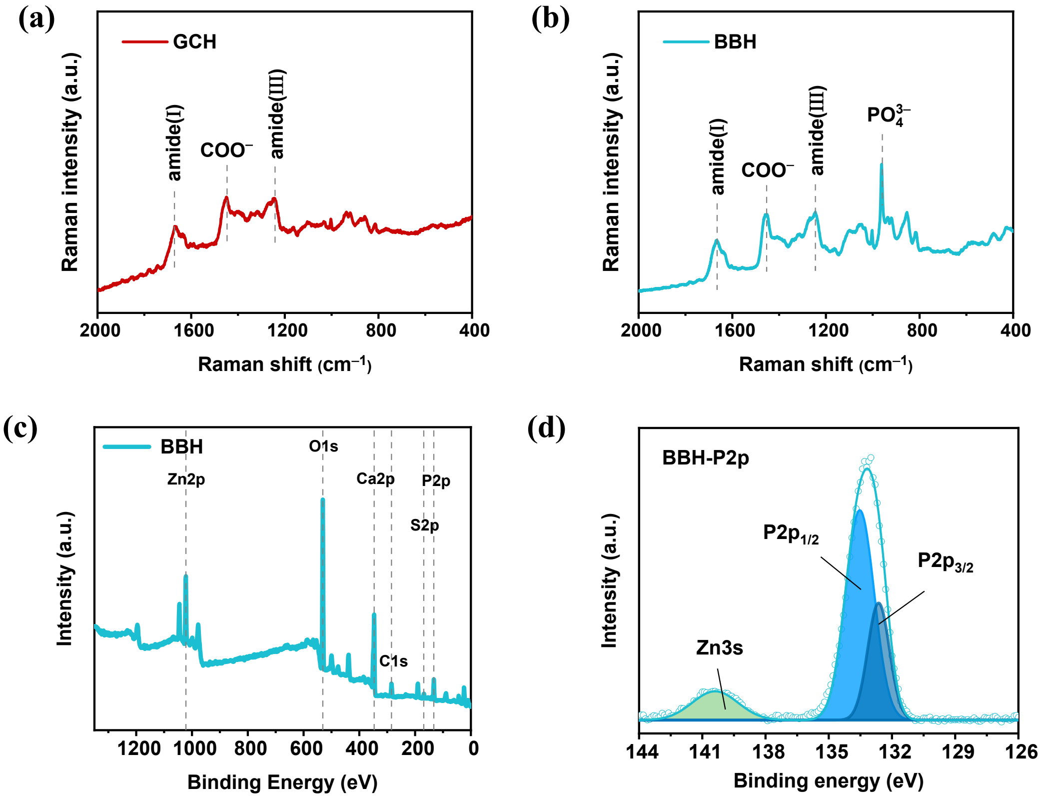

Figure S10. Spectral characterization of GCH, BBH, and BBH electrolytes. Raman spectra of original (a) GCH, and (b) BBH. (c) XPS survey, and (d) XPS P2*p* spectra of BBH electrolyte.

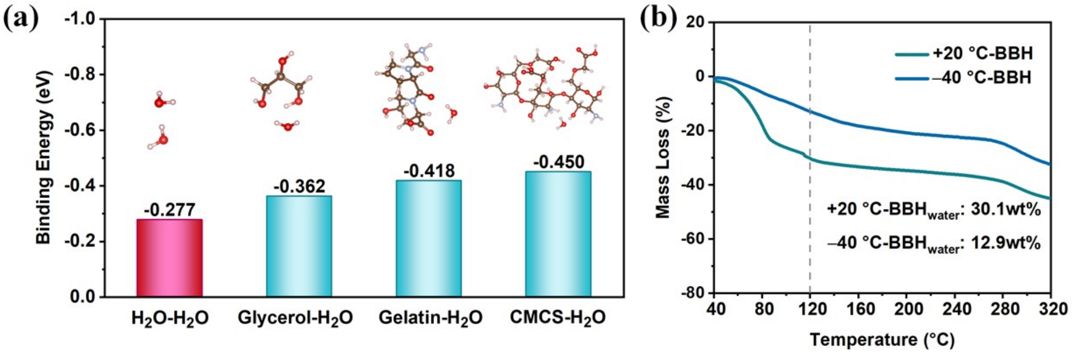

Figure S11. (a) Binding energy between the H_2O and components of BBH. (b) The TGA tests of BBH cross-linked under +20 and -40 °C.

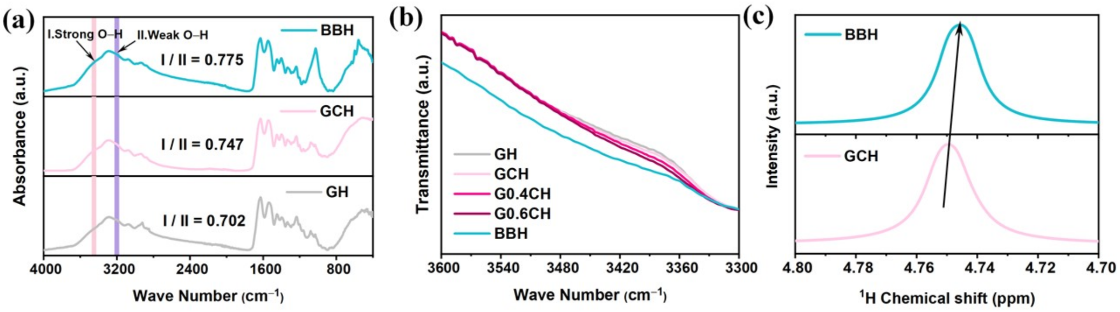

Figure S12. Spectra characterization of O-H bonds of water molecule in different hydrogel systems. (a) ATR-FTIR spectra of GH, GCH, and BBH. (b) ATR-FTIR spectra of BBH, GH, GCH, G0.4CH, and G0.6CH (the adding amounts of CMCS are 0.2, 0, 0.2, 0.4, and 0.6 g, respectively). (c) NMR ^{1}H spectra of GCH and BBH.

In order to compare the hydrogen bond strength between water molecules in different hydrogel systems, we first normalized the infrared spectra. Then the normalized absorption intensity of the peaks at 3600 cm^{-1} and 3200 cm^{-1}, were compared and their ratios were applied to achieve a concise semi-quantitative analysis in Fig. S12a (ESI†)[32]. Since the peaks at these two wave numbers correspond to weak and strong hydrogen bonding interactions between water molecules, their ratios can reflect the regulatory effect of biomimetic densification design on the hydrogen bonding network of water molecules[22, 32, 33].

The O-H bond stretching vibration signals of water molecules in the hydrogel systems with gradient CMCS content were further measured by ATR-FTIR (Fig. S12b, ESI†). It can be seen that, with the increase of CMCS content, the O-H bond strength of water molecules increases. What's more, the O-H bond strength of BBH is further increased compared to G0.6CH, which proves the effectiveness of biomimetic densification design in improving the electrochemical stability window.

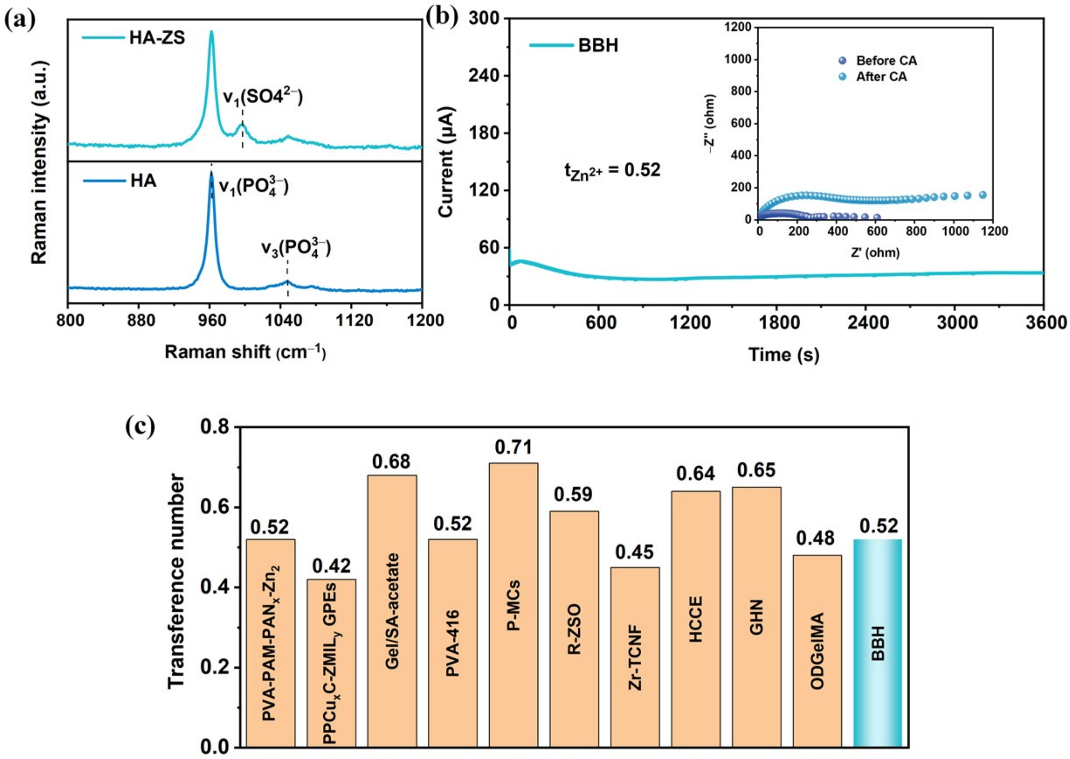

Figure S13. The anions capturing property of HA and transference number of BBH electrolyte. (a) Raman spectra of HA and HA-ZS after ions-exchange for 1 h. (b) Chronoamperometry test of Zn||Zn symmetric cell using BBH electrolyte under 20 mV (Inset: The EIS tests before and after Chronoamperometry test). (c) Comparison of transference number of this work and other reports aiming at advanced hydrogel electrolytes[18, 32, 34-41].

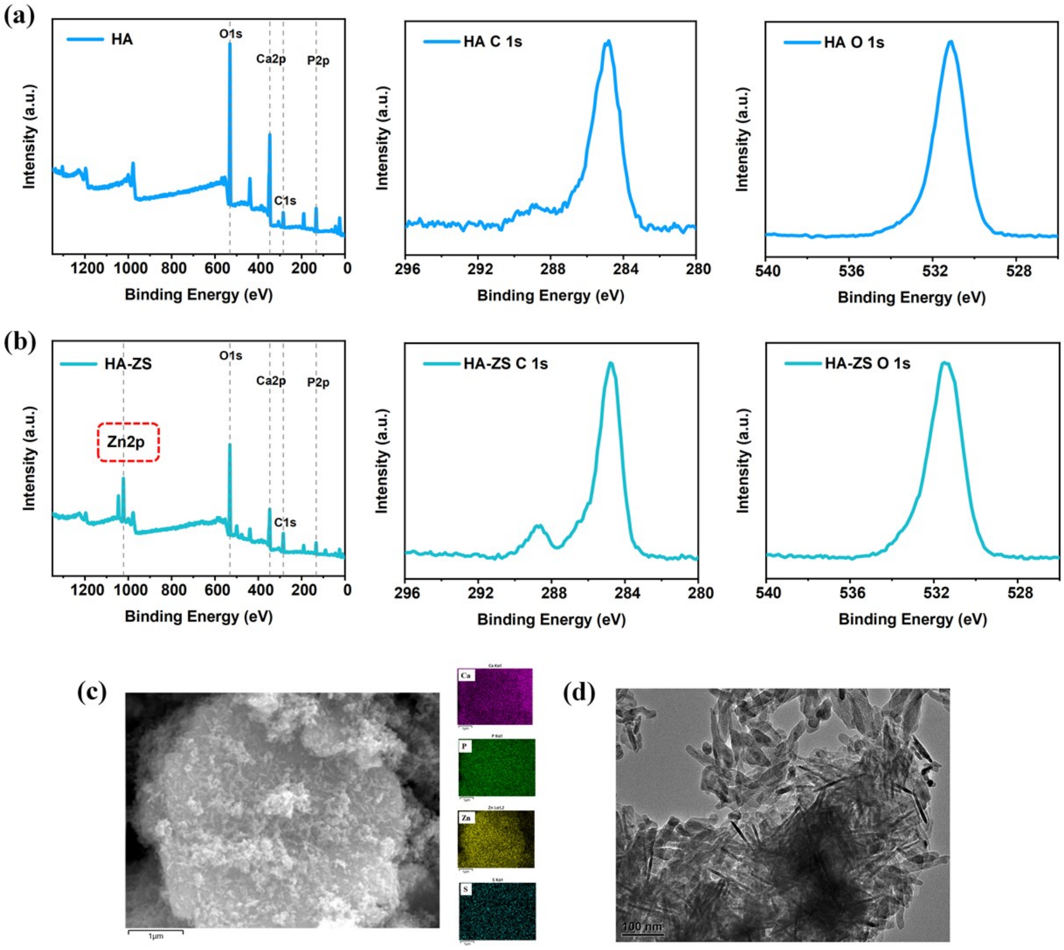

Figure S14. Characterization of the local phase transition triggered by ions exchanged process. XPS spectra and corresponding high-resolution C 1s and O 1s signals analysis of (a) HA, and (b) HA-ZS. (c) SEM images and corresponding EDS mapping of HA-ZS. (d) TEM images of HA-ZS.

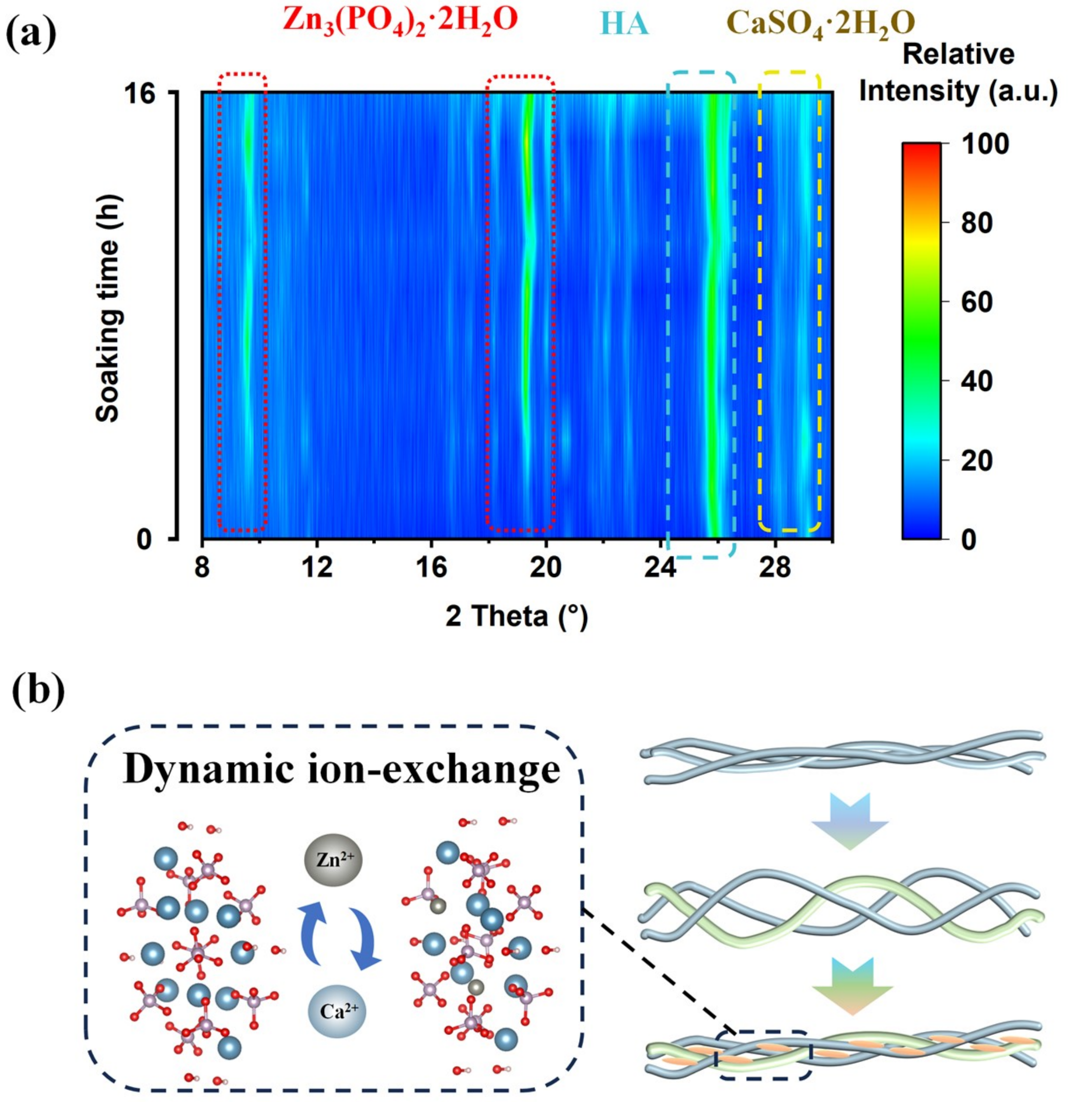

Figure S15. Ion-exchange process of HA with $ZnSO_4$ electrolyte. (a) XRD spectra variation of HA soaked with 3 M $ZnSO_4$ electrolyte along with the soaking time. (b) Mechanism diagram of the ion-exchange process between HA and Zn^{2+} in the BBH structure.

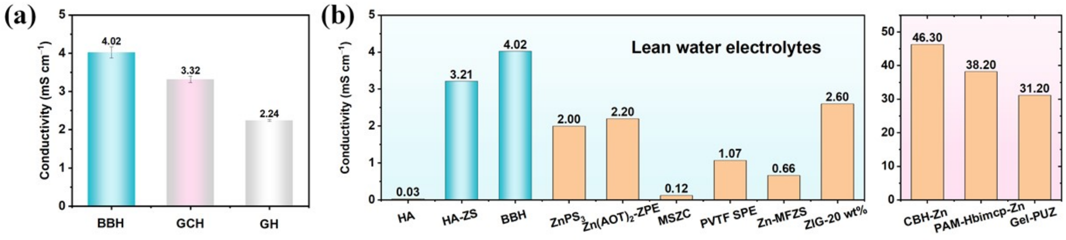

Figure S16. Comparison of ionic conductivities. (a) Conductivities of BBH, GCH, and GH electrolytes. (b) Comparison of conductivities of HA-ZS, BBH electrolytes with other reports aiming at lean liquid or high conductivity electrolytes[33, 42-49].

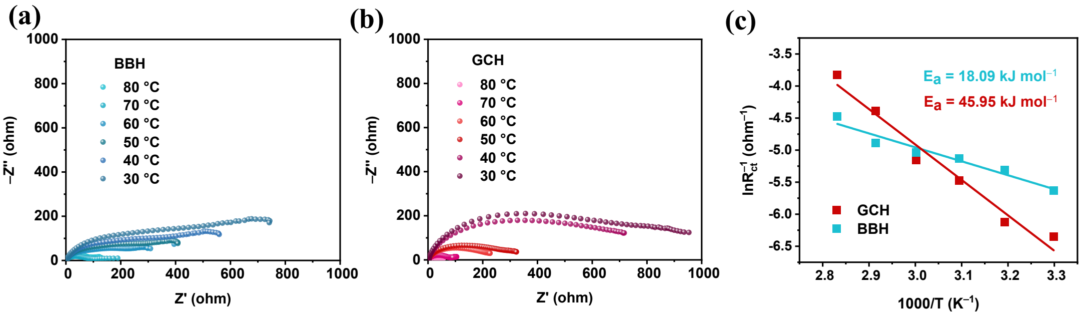

Figure S17. The temperature-dependent EIS tests of the Zn||Zn symmetric cells using (a) BBH and (b) GCH electrolytes. (c) Activation energy E_a based on the fitting of ln R_{ct}^{-1} versus 1000/T Arrhenius curves.

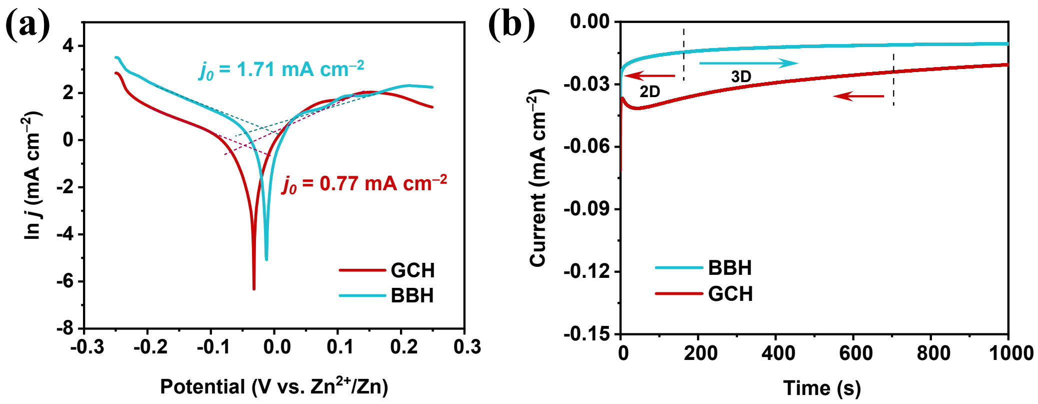

Figure S18. The kinetics of plating/stripping reactions tuned by BBH and GCH electrolytes. (a) Tafel tests. (b) Chronoamperometry tests.

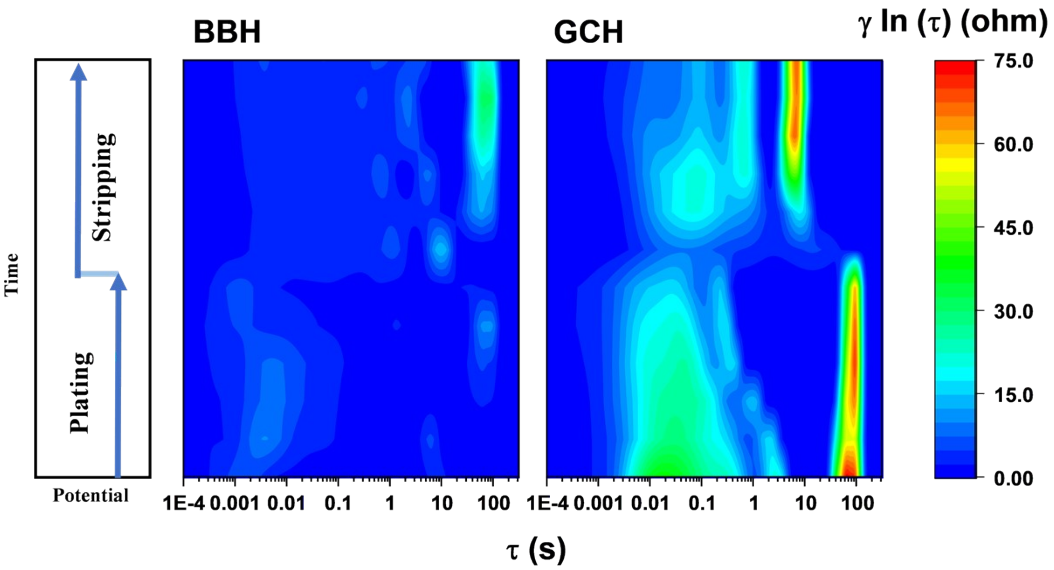

Figure S19. The *in-situ* DRT spectra of Zn||Zn symmetrical cells using BBH and GCH electrolytes at 1 mA cm^{-2}.

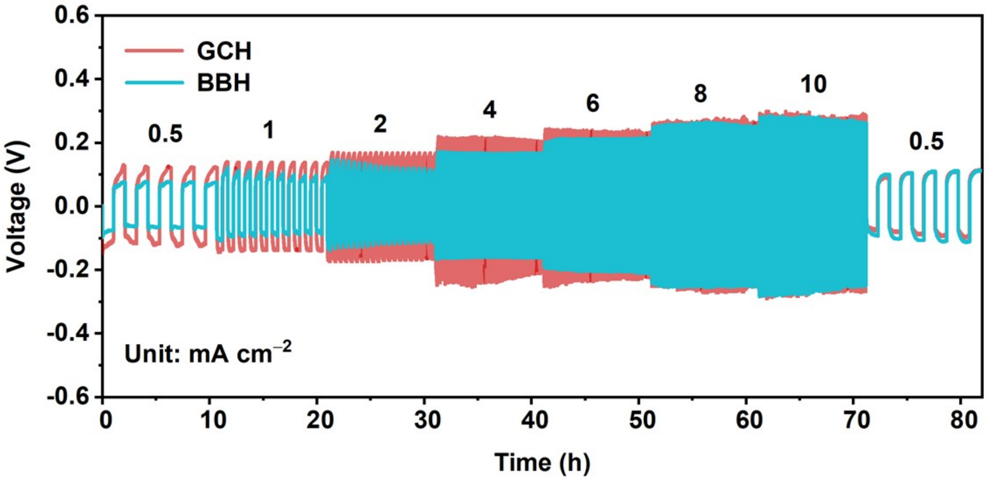

Figure S20. Rate performance of Zn||Zn symmetric cells using GCH and BBH electrolytes.

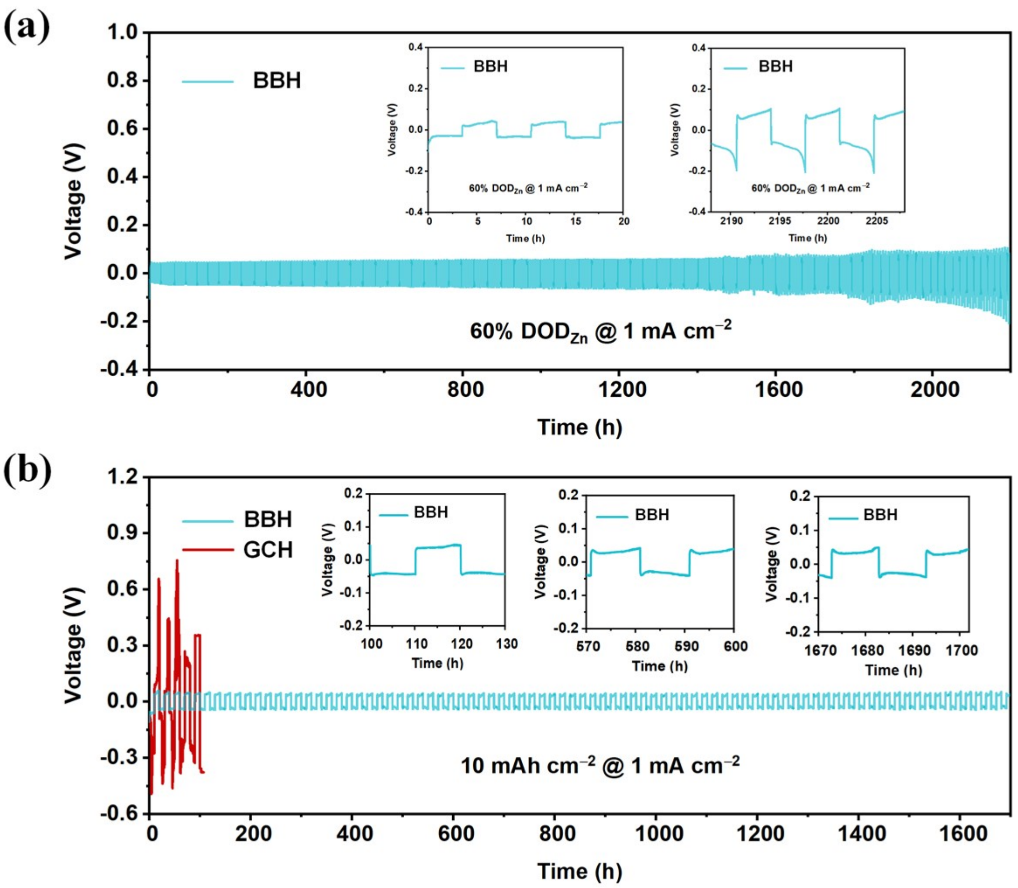

Figure S21. Cyclic performance of Zn||Zn symmetric cells using BBH and GCH electrolytes. (a) 60%DOD$_{Zn}$@1 mA cm^{-2}, (b**)** 10 mAh cm^{-2}@1 mA cm^{-2}.

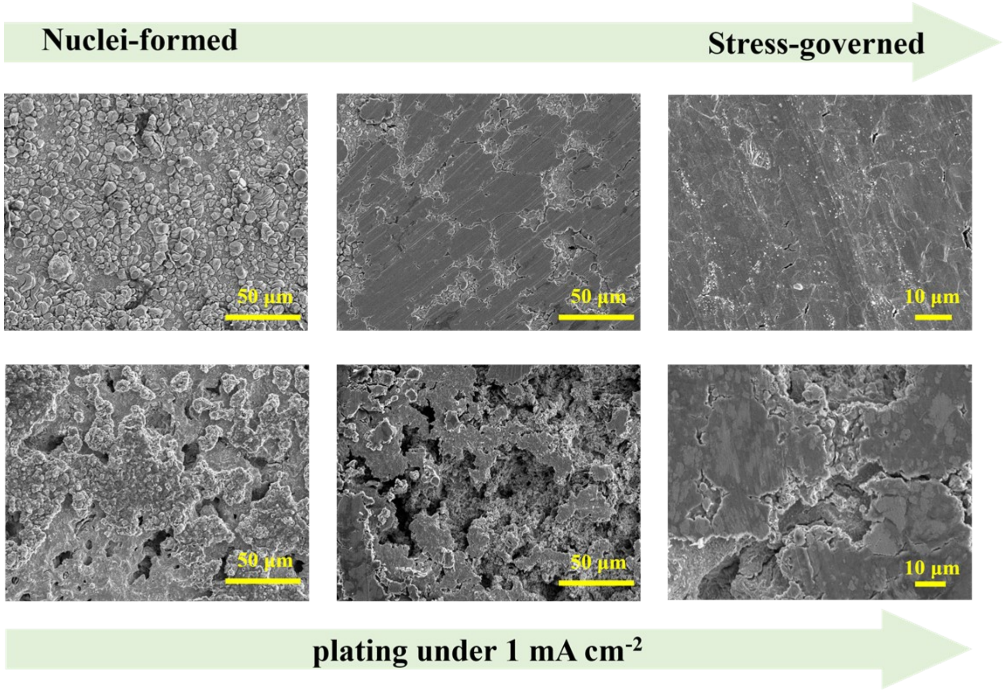

Figure S22. The SEM images of Zn anodes using BBH (top) and GCH electrolytes after plating for 1, 5, and 10 h under 1 mA cm^{-2}.

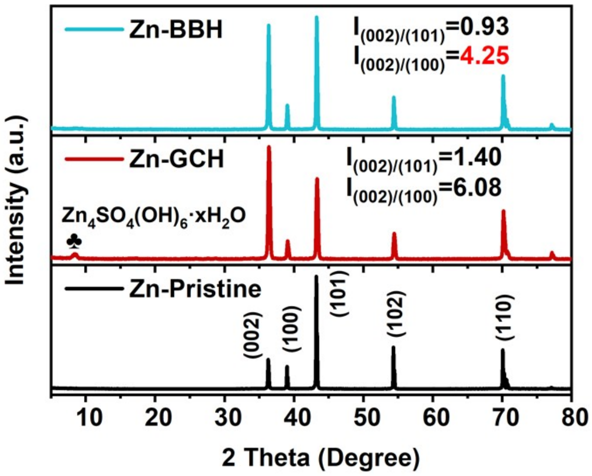

Figure S23. The XRD spectra of Zn anodes using BBH and GCH electrolytes after 50 cycles.

Firstly, according to the previous report[50], introducing additional small molecule components in electrolyte design can cause specific adsorption at the Zn anode interface, thereby affecting the plating orientation. On the other hand, introducing bulk inorganic crystal materials (e.g. $ZnPS_3$, E-nHAP)[42, 51] into electrolyte design can also affect the plating orientation through differences in surface affinity between different crystal planes. Therefore, we believe that the changes in the crystallographic orientation of Zn mainly come from the differences in the components of the GCH and BBH electrolyte. We have summarized the changes in the crystal behavior orientation of Zn anodes after cycling using inorganic coatings such as hydroxyapatite in previous reports[51-53]. The results show that, unlike the common (002) preferred orientation in electrolyte additives design, the introduction of inorganic materials often enhances the preferred orientation of the (101) crystal plane[51-53]. In fact, there have been reports suggesting that other orientations such as the (101) and (100) crystal plane play important roles in corrosion resistance and cycling reversibility[54-57].

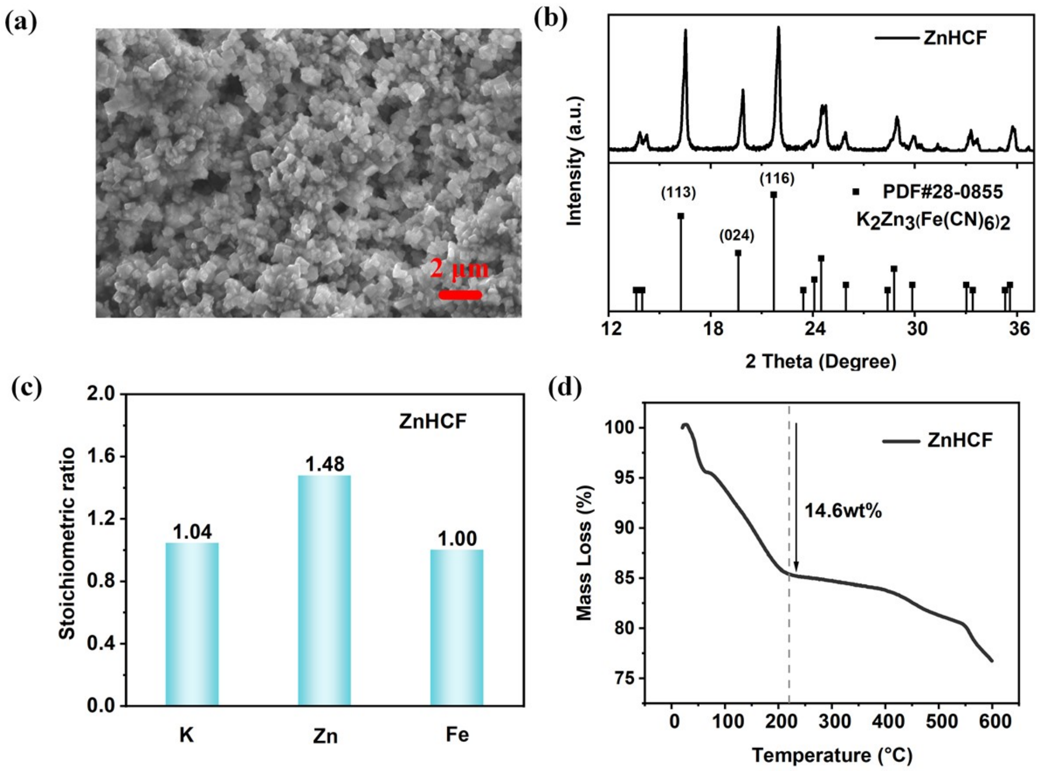

Figure S24. Characterizations of ZnHCF material. (a) SEM images. (b) XRD spectra. (c) ICP-OES test. (d) TGA test.

The specific composition of ZnHCF is determined to be $K_{1.04}Zn_{1.48}[Fe(CN)_6]\cdot 3.31H_2O$ according to the ICP-OES and TGA results. The XRD spectra further reveal that its crystal structure is orthorhombic with space group R-3C. The SEM image reveals that the average particle size of ZnHCF is 0.5-1.0 μm, which is similar to the previous reports[1].

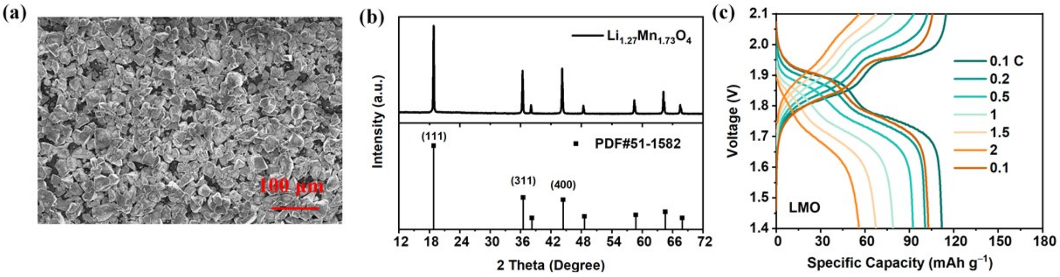

Figure S25. Basic properties of LMO cathodes. (a) SEM images of LMO powder. (b) XRD spectra. (c) Charge and discharge profiles of Zn||LMO full cells using BBH electrolyte**.**

For LMO cathode, the specific composition is $Li_{1.27}Mn_{1.73}O_4$ according to XRD spectra results, which is cubic with space group Fd-3m. The SEM image reveals that the average particle size of LMO is around 50 μm.

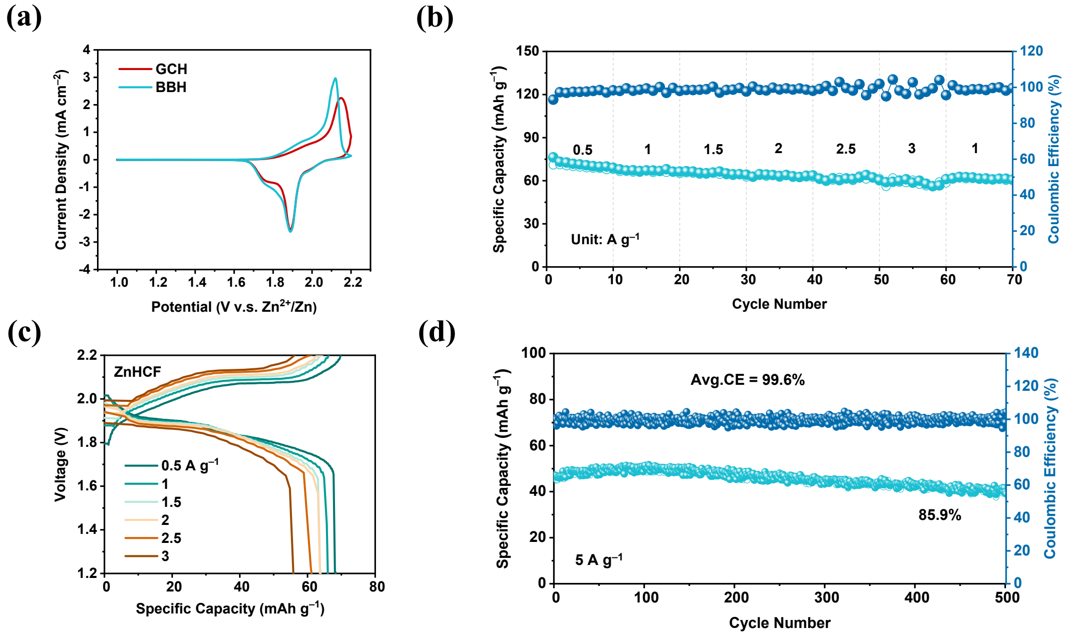

Figure S26. Electrochemical performance of Zn||ZnHCF full cells. (a) CV profiles of Zn||ZnHCF full cells using BBH and GCH electrolytes. (b) Rate performance and corresponding (c) Charge and discharge profiles of Zn||ZnHCF full cells using BBH electrolyte. (d) Cyclic performance at 5 A g^{-1}.

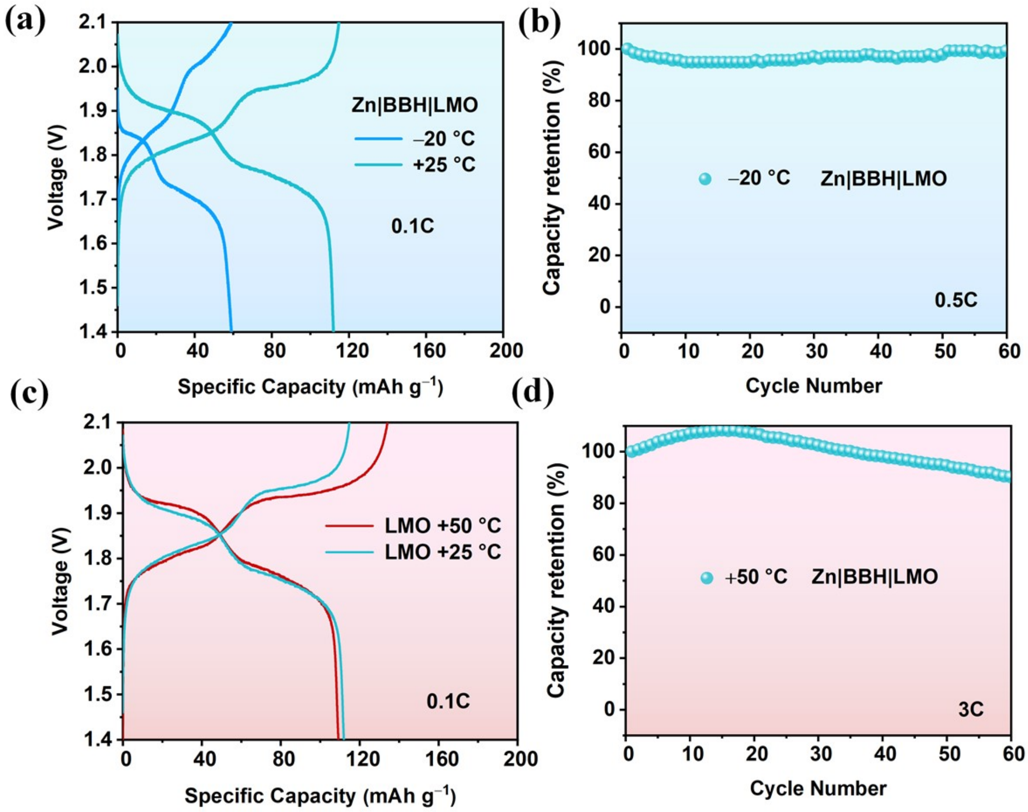

Figure S27. The electrochemical performance of Zn||LMO full batteries using BBH electrolytes under -20/+20/+50 °C. (a) Voltage profiles at 0.1C and -20 °C/+25 °C. (b) Cyclic performance at 0.5C and -20 °C. (c) Voltage profiles at 0.1 C and +50 °C/+25 °C. (d) Cyclic performance at 3C and +50 °C.

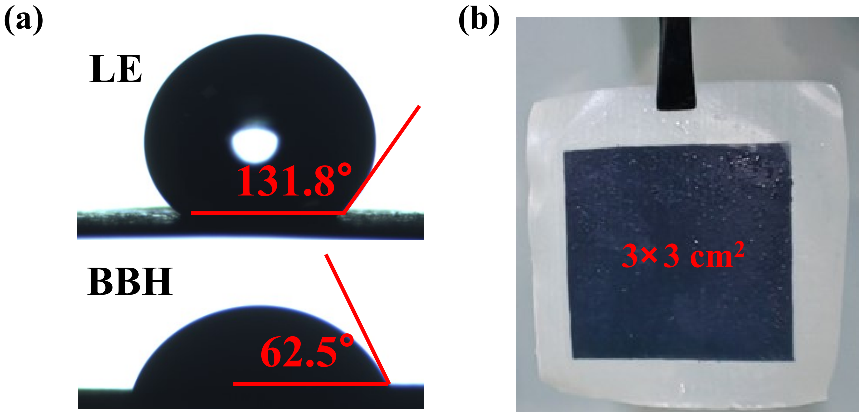

Figure S28. Infiltration of practical-level cathodes. (a) Contact angle tests of practical-level LMO cathodes (35 mg cm^{-2}) with liquid electrolyte (LE) and melting BBH precursor sol. (b) Optical images of seamless and integrated BBH electrolyte/LMO cathode.

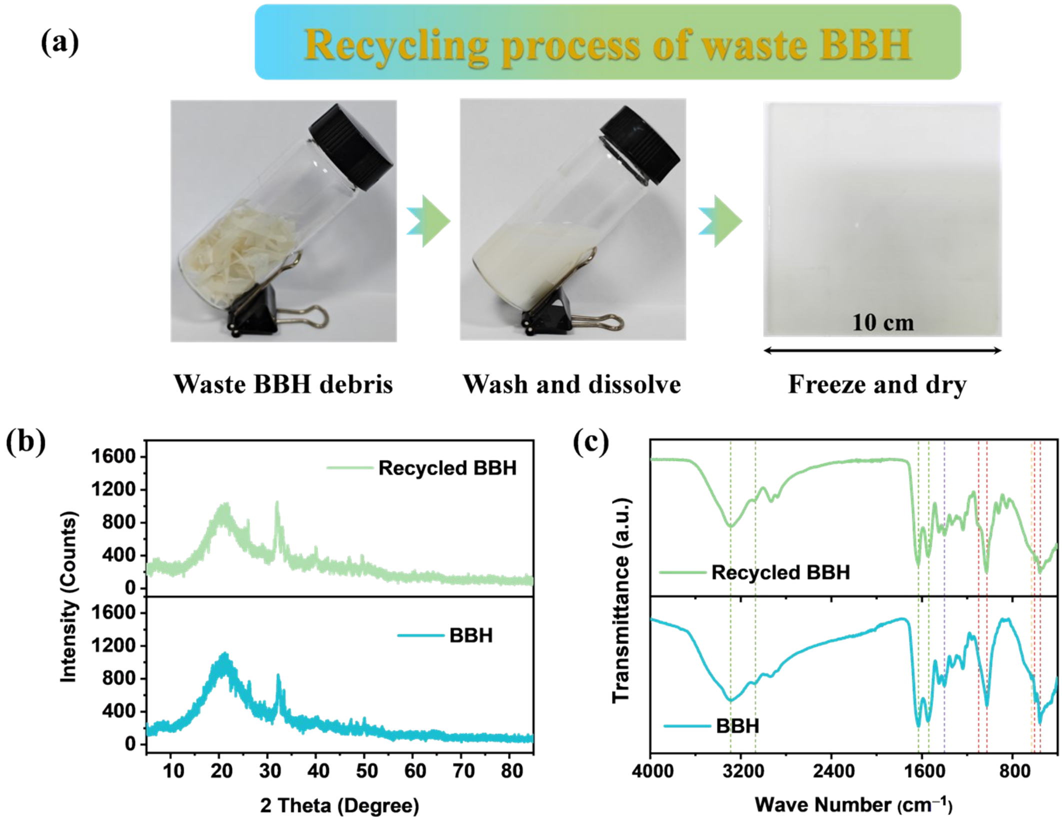

Figure S29. The recycling process and characterizations of Recycled BBH. (a) Recycling process of waste BBH. (b) XRD spectra of original BBH and Recycled BBH. (c) ATR-FTIR spectra of original BBH and Recycled BBH.

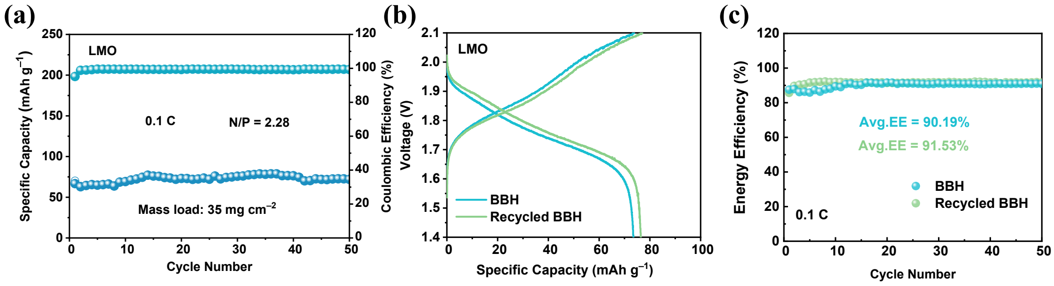

Figure S30. The electrochemical performance of Zn||LMO full cells using Recycled BBH electrolyte. (a) Cyclic performance. (b) Charge and discharge profiles using original BBH and Recycled BBH electrolytes. (c) Energy efficiency of Zn||LMO using original BBH and Recycled BBH electrolytes.

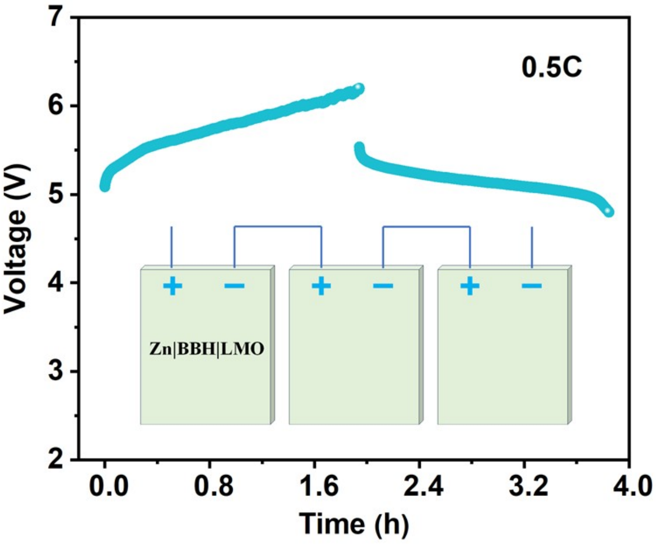

Figure S31. Voltage profiles of practical level Zn||LMO batteries in series.

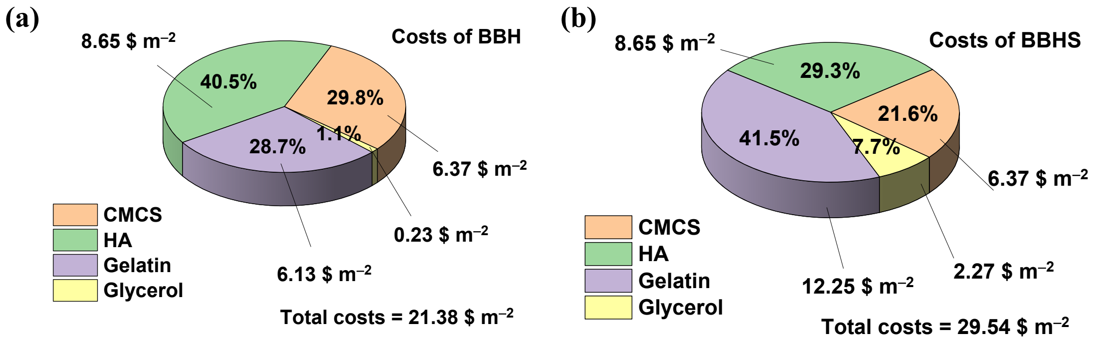

Figure S32. The cost analysis of BBH and BBHS based on the prices of raw material mentioned in the Experimental Section part.

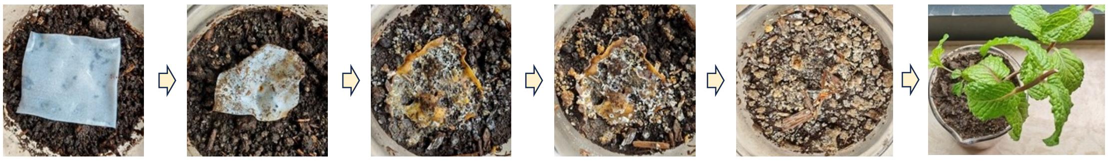

0 day 7 days 14 days 21 days 1 month 1.5 month

Figure S33. Degradation process and environmental friendliness of BBH.

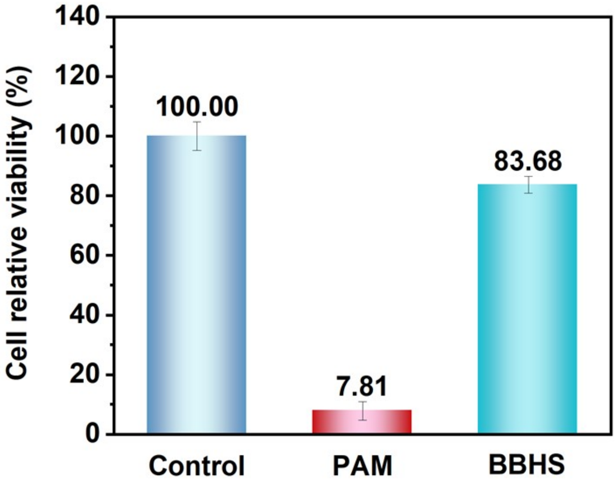

Figure S34. Cell viability of the cells incubated with PAM and BBHS.

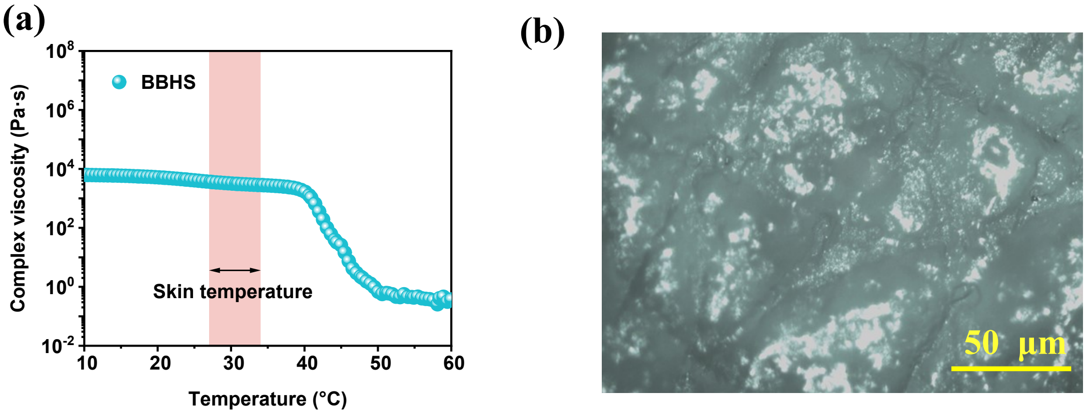

Figure S35. The gelation properties of BBHS as the human/machine interface. (a) Viscosity variation obtained from the rheology test under variable temperature. (b) Optical images of conformal BBHS on the human skin.

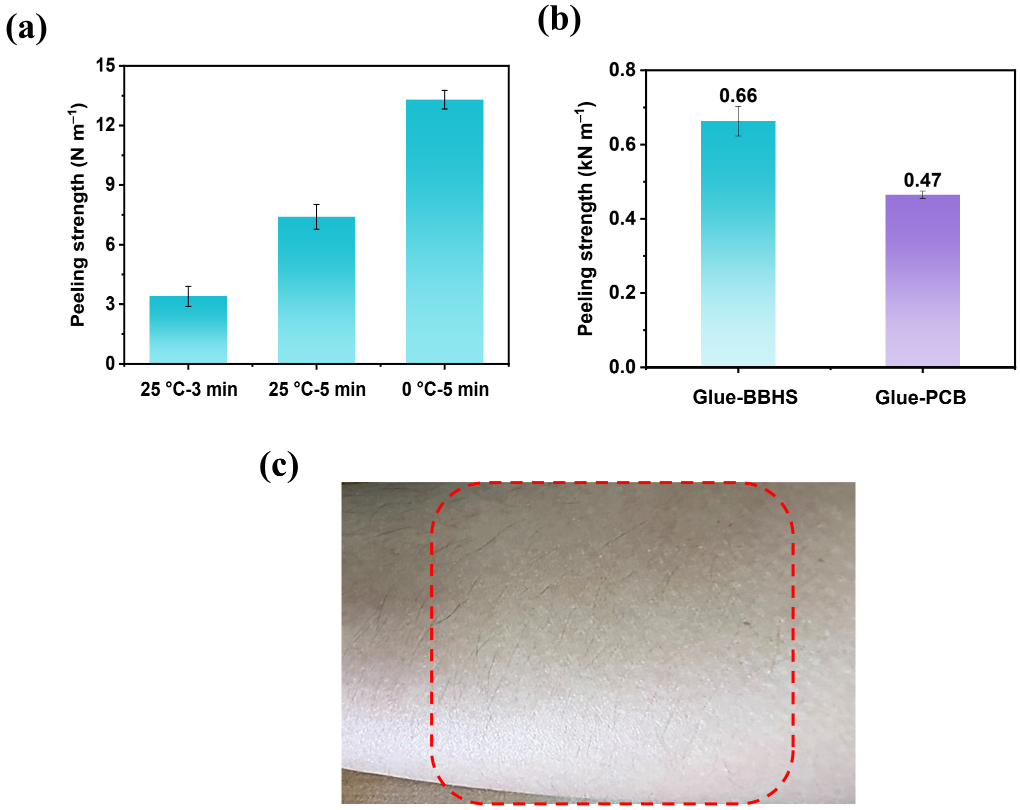

Figure S36. The human/machine interface for temperature and humidity sensing. (a) Peeling strength of BBHS adhering to the human skin under different treatments. (b) Peeling strength among BBHS, pressure-sensitive adhesive, and PCB interface. (c) The optical images of human skin after wearing BBHS.

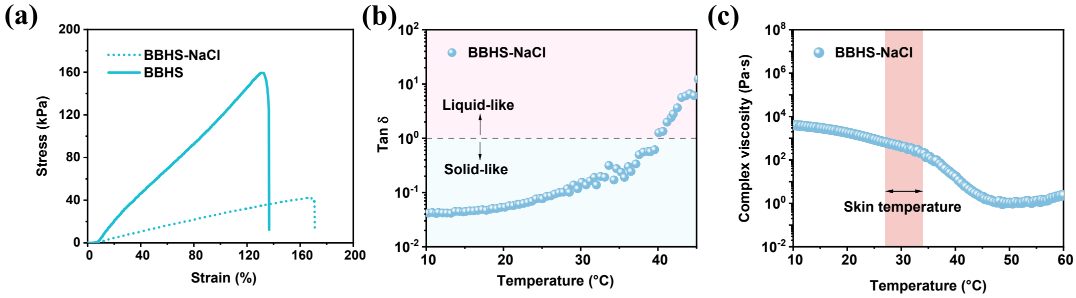

Figure S37. The mechanical properties of BBHS-NaCl as the human/machine interface. (a) Tensile strength of BBHS and BBHS-NaCl. (b) The temperature-variation rheology test of BBHS-NaCl, and (c) viscosity obtained from the rheology test under variable temperature

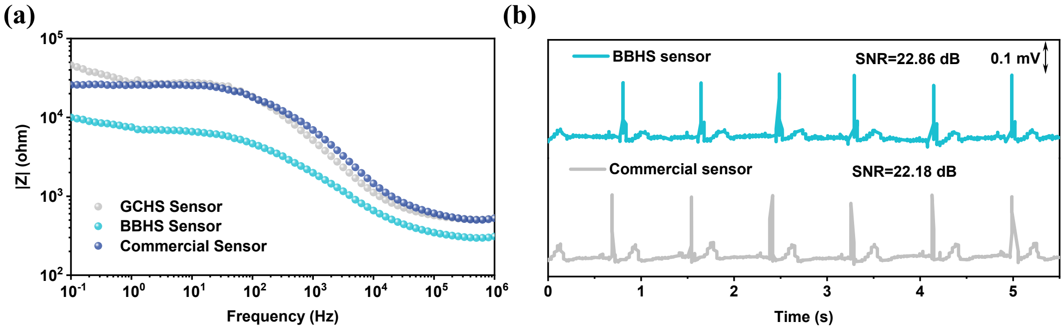

Figure S38. The impedence tests and ECG tests using different sensors. (a) The impedence of different sensors. (b) The ECG signals of BBHS and Commercial Sensor.

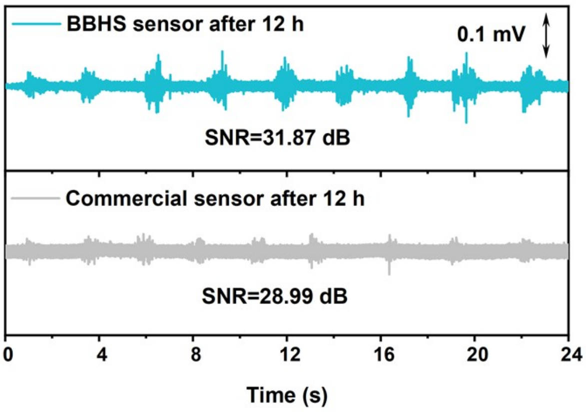

Figure S39. EMG signals based on the BBHS and Commercial sensors after wearing for 12 h.

Table R1 Mechanical and conducting properties of BBH with different contents of CMCS.

CMCS content (g)	Tensile Strength (MPa)	Breaking Elongation (%)	Conductivity (mS cm^{-1})
0.1	20.87	8.33	2.79
0.2	30.82	16.64	4.02
0.3	20.43	17.14	3.42

Table R2 Mechanical and conducting properties of BBH with different contents of HA.

HA content (g)	Tensile Strength (MPa)	Breaking Elongation (%)	Conductivity (mS cm^{-1})
0.1	14.98	18.51	3.31
0.2	30.82	16.64	4.02
0.3	23.94	13.57	2.73

References

1. M. Huang, J. Meng, Z. Huang, X. Wang and L. Mai, *J. Mater. Chem. A*, 2020, **8**, 6631-6637.
2. T. H. Wan, M. Saccoccio, C. Chen and F. Ciucci, *Electrochim. Acta*, 2015, **184**, 483-499.
3. J. F. M., G, W. Trucks, H. B. Schlegel, G. E. Scuseria, M. A. Robb, J. R. Cheeseman, G. Scalmani, V. Barone, B. Mennucci and G. A. Petersson, 2009.
4. P. C. Hariharan and J. A. Pople, *Mol. Phys.*, 1974, **27**, 209-214.
5. G. A. Petersson, A. Bennett, T. G. Tensfeldt, M. A. Al-Laham, W. A. Shirley and J. Mantzaris, *J. Chem. Phys.*, 1988, **89**, 2193-2218.
6. A. V. Marenich, C. J. Cramer and D. G. Truhlar, *J Phys Chem B*, 2009, **113**, 6378-6396.
7. G. Kresse and J. Furthmüller, *Computational Materials Science*, 1996, **6**, 15-50.
8. M. W. H. Kirkness, K. Lehmann and N. R. Forde, *Current Opinion in Chemical Biology*, 2019, **53**, 98-105.
9. Y. He, C. Wang, C. Wang, Y. Xiao and W. Lin, *Polymers*, 2021, **13**, 2299.
10. C.-A. Dai and M.-W. Liu, *Materials Science and Engineering: A*, 2006, **423**, 121-127.
11. C. Qiao, X. Ma, J. Zhang and J. Yao, *Food Chemistry*, 2017, **235**, 45-50.
12. S. Sethi, Medha and B. S. Kaith, *Reactive and Functional Polymers*, 2022, **179**, 105362.
13. H.-W. Kang, Y. Tabata and Y. Ikada, *Biomaterials*, 1999, **20**, 1339-1344.
14. J. Grenier, H. Duval, F. Barou, P. Lv, B. David and D. Letourneur, *Acta Biomaterialia*, 2019, **94**, 195-203.
15. S. Van Vlierberghe, V. Cnudde, P. Dubruel, B. Masschaele, A. Cosijns, I. De Paepe, P. J. S. Jacobs, L. Van Hoorebeke, J. P. Remon and E. Schacht, *Biomacromolecules*, 2007, **8**, 331-337.
16. X. Liu and P. Cheng, *International Journal of Heat and Mass Transfer*, 2015, **83**, 833-841.
17. C. Li, W. Wang, J. Luo, W. Zhuang, J. Zhou, S. Liu, L. Lin, W. Gong, G. Hong, Z. Shao, J. Du, Q. Zhang and Y. Yao, *Adv. Mater.*, 2024, **36**, 2313772.
18. Y. Yan, S. Duan, B. Liu, S. Wu, Y. Alsaid, B. Yao, S. Nandi, Y. Du, T.-W. Wang, Y. Li and X. He, *Adv. Mater.*, 2023, **35**, 2211673.
19. G. Cao, L. Zhao, X. Ji, Y. Peng, M. Yu, X. Wang, X. Li and F. Ran, *Small*, 2023, **19**, 2207610.
20. L. Wan, H. Zhang, M. Qu, M. Feng, Z. Shang, R. Wang, D. Lei and Y. Cui, *Energy Storage Mater.*, 2023, **63**, 102982.
21. M. Chen, J. Chen, W. Zhou, X. Han, Y. Yao and C.-P. Wong, *Adv. Mater.*, 2021, **33**, 2007559.
22. D. Feng, Y. Jiao and P. Wu, *Angew. Chem. Int. Ed.*, 2023, **62**, e202215060.
23. X. Zhang, J. Li, K. Qi, Y. Yang, D. Liu, T. Wang, S. Liang, B. Lu, Y. Zhu and J. Zhou, *Adv. Mater.*, 2022, **34**, 2205175.
24. H. Yang, R. Zhu, Y. Yang, Z. Lu, Z. Chang, P. He, C. Zhu, S. Kitano, Y. Aoki, H. Habazaki and H. Zhou, *Energy Environ. Sci.*, 2023, **16**, 2133-2141.
25. L. Yao, C. Hou, M. Liu, H. Chen, Q. Zhao, Y. Zhao, Y. Wang, L. Liu, Z.-W. Yin, J. Qiu, S. Li, R. Qin and F. Pan, *Adv. Funct. Mater.*, 2023, **33**, 2209301.
26. L. Lan, J. Ping, H. Li, C. Wang, G. Li, J. Song and Y. Ying, *Adv. Mater.*, 2024, **n/a**, 2401151.
27. S. Sun, Y. Xu and X. Maimaitiyiming, *International Journal of Biological Macromolecules*, 2023, **249**, 125978.
28. D. Wang, J. Zhang, C. Fan, J. Xing, A. Wei, W. Xu, Q. Feng and Q. Wei, *Composites Part B: Engineering*, 2022, **243**, 110116.
29. A. A. Salifu, C. Lekakou and F. H. Labeed, *Journal of Biomedical Materials Research Part A*, 2017, **105**, 1911-1926.
30. L. Cao, Z. Zhao, X. Wang, X. Huang, J. Li and Y. Wei, *Advanced Materials Technologies*, 2022, **7**, 2101382.
31. M. Baumgartner, F. Hartmann, M. Drack, D. Preninger, D. Wirthl, R. Gerstmayr, L. Lehner, G. Mao, R. Pruckner, S.

Demchyshyn, L. Reiter, M. Strobel, T. Stockinger, D. Schiller, S. Kimeswenger, F. Greibich, G. Buchberger, E. Bradt, S. Hild, S. Bauer and M. Kaltenbrunner, *Nature Materials*, 2020, **19**, 1102-1109.

32. C. Tian, J. Wang, R. Sun, T. Ali, H. Wang, B.-B. Xie, Y. Zhong and Y. Hu, *Angew. Chem. Int. Ed.*, 2023, **62**, e202310970.
33. X. Zhou, S. Huang, L. Gao, Z. Zhang, Q. Wang, Z. Hu, X. Lin, Y. Li, Z. Lin, Y. Zhang, Y. Tang, Z. Wen, M. Ye, X. Liu and C. C. Li, *Angew. Chem. Int. Ed.*, 2024, **63**, e202410434.
34. S. Yang, Y. Zhang, Y. Zhang, J. Deng, N. Chen, S. Xie, Y. Ma and Z. Wang, *Adv. Funct. Mater.*, 2023, **33**, 2304280.
35. J. Hu, Y. Qu, F. Shi, J. Wang, X. He, S. Liao and L. Duan, *Adv. Funct. Mater.*, 2022, **32**, 2209463.
36. J. Kumankuma-Sarpong, C. Chang, J. Hao, T. Li, X. Deng, C. Han and B. Li, *Adv. Mater.*, 2024, **36**, 2403214.
37. Y. Cui, W. Chen, W. Xin, H. Ling, Y. Hu, Z. Zhang, X. He, Y. Zhao, X.-Y. Kong, L. Wen and L. Jiang, *Adv. Mater.*, 2024, **36**, 2308639.
38. F. Luo, S. Yang, Q. Wu, Y. Li, J. Zhang, Y. Zhang, J. Huang, H. Xie and Y. Chen, *Energy Environ. Sci.*, 2024, **17**, 8570-8581.
39. J. Gao, X. Xie, S. Liang, B. Lu and J. Zhou, *Nano-Micro Letters*, 2021, **13**.
40. H. R. Wang, A. B. Zhou, Z. Q. Hu, X. Hu, F. L. Zhang, Z. H. Song, Y. X. Huang, Y. H. Cui, Y. X. Cui, L. Li, F. Wu and R. J. Chen, *Angewandte Chemie-International Edition*, 2024, **63**.
41. Z.-J. Chen, T.-Y. Shen, X. Xiao, X.-C. He, Y.-L. Luo, Z. Jin and C.-H. Li, *Adv. Mater.*, **n/a**, 2413268.
42. Z. Lv, Y. Kang, G. Chen, J. Yang, M. Chen, P. Lin, Q. Wu, M. Zhang, J. Zhao and Y. Yang, *Adv. Funct. Mater.*, 2024, **34**, 2310476.
43. Z. Zhao, B. Nian, Y. Lei, Y. Wang, L. Shi, J. Yin, O. F. Mohammed and H. N. Alshareef, *Adv. Energy Mater.*, 2023, **13**, 2300063.
44. J. Wang, Z. Zhao, G. Lu, Y. Zhang, Q. Kong, J. Zhao and G. Cui, *Materials Today Energy*, 2021, **20**, 100630.
45. Y. Hou, Z. Wei, Z. Wu, Y. Wang, Z. Huang, Q. Li, Z. Chen, X. Li, P. Li, H. Cui, G. Liang and C. Zhi, *Energy Environ. Sci.*, 2024, **17**, 3917-3926.
46. J. Zhi, S. Zhao, M. Zhou, R. Wang and F. Huang, *Science Advances*, 2023, **9**, eade2217.
47. Y. Wang, Q. Li, H. Hong, S. Yang, R. Zhang, X. Wang, X. Jin, B. Xiong, S. Bai and C. Zhi, *Nat. Commun.*, 2023, **14**, 3890.
48. J. Lu, X. Lin, S. Wang, X. Xu, Y. Zhou, Y. Zhang, Q. Li and H. Liu, *Green Chemistry*, 2023, **25**, 1635-1646.
49. Z.-J. Chen, T.-Y. Shen, M.-H. Zhang, X. Xiao, H.-Q. Wang, Q.-R. Lu, Y.-L. Luo, Z. Jin and C.-H. Li, *Adv. Funct. Mater.*, 2024, **34**, 2314864.
50. Y. Lin, Y. Li, Z. Mai, G. Yang and C. Wang, *Adv. Energy Mater.*, 2023, **13**, 2301999.
51. K. Qi, W. Zhu, X. Zhang, M. Liu, H. Ao, X. Wu and Y. Zhu, *ACS Nano*, 2022, **16**, 9461-9471.
52. Q. Zou, Z. Liang, W. Wang, D. Dong and Y.-C. Lu, *Energy Environ. Sci.*, 2023, **16**, 6026-6034.
53. Z. Xing, G. Xu, X. Xie, M. Chen, B. Lu, J. Zhou and S. Liang, *Nano Energy*, 2021, **90**, 106621.
54. L. Ren, Z. Hu, C. Peng, L. Zhang, N. Wang, F. Wang, Y. Xia, S. Zhang, E. Hu and J. Luo, *Proceedings of the National Academy of Sciences*, 2024, **121**, e2309981121.
55. Z. Liu, Z. Guo, L. Fan, C. Zhao, A. Chen, M. Wang, M. Li, X. Lu, J. Zhang, Zhang, Yu and N. Zhang, *Adv. Mater.*, 2024, **36**, 2305988.
56. Y. Wang, J. Lv, L. Hong, J. Zhang, C. Chen, A. Xu, M. Huang, X. Ren, J. Bai, H. Wang and X. Liu, *Angew. Chem. Int. Ed.*, **n/a**, e202414757.
57. Z. Cheng, K. Wang, J. Fu, F. Mo, P. Lu, J. Gao, D. Ho, B. Li and H. Hu, *Adv. Energy Mater.*, 2024, **14**, 2304003.